Bioelectrochemistry 155 (2024) 108573

Contents lists available at ScienceDirect

Bioelectrochemistry

journal homepage: www.journals.elsevier.com/bioelectrochemistry

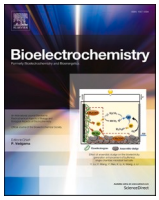

Unraveling the kinetics and pharmacology of human PepT1 using solid supported membrane-based electrophysiology

Alexander Körner [a,b,1], Andre Bazzone [c,1], Maximilian Wichert [a,d], Maria Barthmes [c], Srujan Kumar Dondapati [a,*], Niels Fertig [c], Stefan Kubick [a,d,e]

[a] Fraunhofer Institute for Cell Therapy and Immunology (IZI), Branch Bioanalytics and Bioprocesses (IZI-BB), Am Mühlenberg 13, 14476 Potsdam, Germany
[b] Institute of Biotechnology, Technische Universität Berlin, Straße des 17. Juni 135, 10623 Berlin, Germany
[c] Nanion Technologies GmbH, Ganghoferstr. 70a, 80339 Munich, Germany
[d] Freie Universität Berlin, Institute of Chemistry and Biochemistry – Biochemistry, 14195 Berlin, Germany
[e] Faculty of Health Sciences, Joint Faculty of the Brandenburg University of Technology Cottbus – Senftenberg, The Brandenburg Medical School Theodor Fontane and the University of Potsdam, Germany

ARTICLE INFO

Keywords:
Membrane transport
Peptide Transporter 1 (PepT1)
Solid Supported Membrane-based Electrophysiology (SSME)
Biosensor
Pharmacology
High-throughput screening (HTS)

ABSTRACT

The human Peptide Transporter 1 (hPepT1) is known for its broad substrate specificity and its ability to transport (pro-)drugs. Here, we present an in-depth comprehensive study of hPepT1 and its interactions with various substrates via solid supported membrane-based electrophysiology (SSME). Using hPepT1-containing vesicles, we could not identify any peptide induced pre-steady-state currents, indicating that the recorded peak currents reflect steady-state transport. Electrogenic co-transport of H^+/glycylglycine (GlyGly) was observed across a pH range of 5.0 to 9.0. The pH dependence is described by a bell-shaped activity curve and two pK values. K_M and relative V_{max} values of various canonical and non-canonical peptide substrates were contextualized with current mechanistic understandings of hPepT1. Finally, specific inhibition was observed for various inhibitors in a high throughput format, and IC50 values are reported. Taken together, these findings contribute to promoting the design and analysis of pharmacologically relevant substances.

1. Introduction

Solute carriers are not only therapeutic targets for a variety of diseases, but also key factors in drug delivery. Poor oral bioavailability is a major bottleneck in drug development [1]. Hence, many (pro-) drugs target or are modified to target transporters expressed in the intestine, such as the solute carrier family 15 member 1 (SLC15A1), also known as peptide transporter 1 (PepT1). In humans, PepT1 plays an important physiological and pharmacological role [2,3]. It mediates the electrogenic co-transport of mono- or polyvalently charged di- & tripeptides but also peptidomimetic substances [1], among which - as partially referred to in [4] - a plethora of drugs and prodrugs is found [5–7], e.g. ACE inhibitors, the antibiotics cefadroxil and cefprozil [8,9], antivirals such as valaciclovir [10], protease inhibitor bestatin [11] and some anticancer drugs [12].

PepT1 belongs to the larger Proton-dependent Oligopeptide Transporter (POT) family of secondary active transporters, which uses an inwardly directed H^+ gradient to drive uptake [13,14]. POT-mediated transport works via alternating access of the substrate binding sites [15–17]: In brief, the outward facing empty carrier opens to accept protons, and the peptide becomes occluded, transitions inward, opens up, releases its load, before the empty inward-facing open carrier returns to its outward-facing state.

The electrogenicity of H^+/peptide cotransport in PepT1 makes it amenable to electrophysiological approaches such as Giant Patch Clamp (GPC) and Two-electrode voltage-clamp (TEVC). These methods have been extensively used to study the electrogenic transport of PepT1, revealing its substrate promiscuity, bidirectionality, and the phenomenon of *trans*-stimulation [18]. Uncovering kinetic features such as the pH and voltage dependency of substrate affinities contributes to the understanding of the fundamental properties of this protein. However, this process is far from complete to date. To address questions about the forces that determine substrate specificity and turnover limitations, it is necessary to conduct studies that properly contextualize these

* Corresponding author.
E-mail address: Srujan.Dondapati@izi-bb.fraunhofer.de (S.K. Dondapati).
[1] The author contributed to the work equally and should be regarded as co-first author.

https://doi.org/10.1016/j.bioelechem.2023.108573
Received 17 July 2023; Received in revised form 14 September 2023; Accepted 15 September 2023
Available online 16 September 2023

phenomena.

Despite the numerous advantages of conventional electrophysiology, solid supported membrane-based electrophysiology (SSME) helps to approach transport mechanisms from a different angle. Since currents are induced by substrate concentration jumps, reaction steps induced by substrate binding may be resolved as pre steady-state currents as we recently demonstrated for the Na^+/sugar cotransporter SGLT1 [19,20]. Due to the voltage-independent transport initiation, there are no relevant leak currents that may complicate the analysis [21]. SSME is increasingly established within transporter research. Exposing the carrier to its substrates via solution exchange initiates the transport that is recorded in real-time (Fig. 1B). The accumulative measurement of transporters from millions of proteoliposomes produces enormous signal amplification compared to patch-clamp setups where the cell surface limits the signal-to-noise ratio [22]. Applying SSME for hPepT1 and orthologues as well as amino acid transporters has been highlighted in recent publications [23–26], yet, a comprehensive in-depth study is still missing.

Here, we used this technology to measure signals from cell-derived membrane vesicles and observe the pH dependence of H^+/glycylglycine (GlyGly) cotransport, and determined kinetic parameters for a range of canonical and non-canonical substrates as well as inhibitors. We investigated peptide-induced hPepT1 currents in real-time and concluded information about electrogenic steps within the transport cycle. Finally, we integrate our findings into current models and understandings of hPepT1.

2. Material and methods

2.1. Material

The following substrates and inhibitors were obtained (supplier, product number). Glibenclamide (Sigma-Aldrich, G0639), Glycyl-L-glycine (Sigma-Aldrich, 50199), Glycyl-glycyl-glycine (Merck, G1377), Glycyl-L-aspartic acid (Merck, 50170), Glycyl-L-glutamate (Merck, G0877), Glycyl-L-glutamine monohydrate (ABCR, AB 314221), Glycyl-L-phenylalanine (Merck, G2752), Glycyl-L-Sar (ABCR, AB 136426), Glycyl-L-tyrosine (hoelzel biotech, HY-W009592), Glycyl-L-valine (ABCR, AB 136426), L-Alanyl-L-1-amino-ethanphosphonic acid "Alafosalin" (Sigma-Aldrich, 5260), Valacyclovir hydrochloride (Sigma-Aldrich, PHR1601), Zinc chloride (Sigma-Aldrich, 793523). Lys[Z(NO2)]-Val × TFA was synthesized by SynphaBase AG (Switzerland) (Lot. Nr. 1833-CA/2).

3. Methods

3.1. Cultivation of overexpressing cells

CHO-PepT1 overexpressing cells were cultivated at 37 °C under 5% CO_2 with DMEM without pyruvate (Biochrom) + 10% Fetal calf serum, 2 mM alanyl-glutamine, 200 μg/ml Hygromycin B (VWR Ultrapure), 200 μg/ml Geneticin (VWR) until 40% confluency. Medium was renewed, and 1 μg/ml tetracycline was added for induction. After 24 h further incubation (at roughly 80–90% confluency), cells were ready for harvest. Control cells (CHO-K1) were not subjected to any antibiotics, but otherwise treated alike.

3.2. Preparation of cellular membrane vesicles

Cells were grown in 15 cm dishes and were induced 24 h prior to harvest. Cells were washed once with PBS and once with PBS + 0.05 % EDTA, before being detached by incubation with harvesting buffer (PBS, EDTA, 1 tablet of cOmplete protease inhibitor per 50 ml) for 10 min at 37 °C. Cells were pooled (roughly 1 g), centrifuged for 10 min at 4 °C, 1,000 g, and pellets frozen in liquid nitrogen and stored at −80 °C until further treatment / disruption.

For cell disruption via nitrogen decompression, pellets were thawed and re-suspended in 30 ml lysis buffer (Saccharose 8.6% (w/V), 10 mM Tris pH 7.4), and transferred into the Parr Instrument disruption vessel. 70 bar nitrogen was applied for 20 min. Pressure was cautiously released, and the lysate harvested. After removal of crude debris (4,500 g, 4 °C, 10 min), membranes were pelleted using ultracentrifugation (100,000 g, 4 °C, 30 min, Type 50 Ti rotor). Pellet was re-suspended in 1 ml lysis buffer, sample was brought to 51% sucrose by adding 2.22 volumes of 70% sucrose. Sequentially, 9 ml of 45% sucrose, 9 ml of 31% sucrose, and 3 ml of 9% sucrose were carefully added on top. Sucrose gradient was centrifuged (100,000 g, 4 °C, ≥ 3 h, Swing Bucket Rotor SW 32 Ti). Interfaces between 9% and 31% sucrose, and 31% and 45% sucrose were collected independently, and washed (100,000 g, 4 °C, 30 min, Type 50 Ti rotor). Pelleted membranes were re-suspended in storage buffer (140 mM NaCl, 2 mM $MgCl_2$, 30 mM Tris/HCl pH 7.5, 5% Glycerol). 10 μl aliquots with protein concentrations of ~ 1 – 6 μg/μl were frozen via liquid nitrogen, and stored at -80 °C.

3.3. Sample preparation for Western Blot

Frozen cell pellets (CHO K1 (neg), CHO hPepT1 overexpressing cells; roughly 80 mg each) were thawed on ice and re-suspended in 1 ml RIPA buffer. Mixture was incubated for at least 15 min on ice with vortexing every 5 min. Solution was centrifuged for 15 min at 14,000x g, 4 °C and supernatant was transferred to a new reaction tube. Protein concentration was determined with BCA protein assay kit (ThermoFisher).

3.4. PNGaseF digest (Orientation assay)

1 μl of cell patches were diluted in 19 μl H_2O. 5 μl of diluted samples were mixed with 1 μl of GlycoBuffer 2 and 4 μl H_2O. Then 1 μl of PNGase F (NEB) was added. Reaction was incubated for 19 h at 37 °C. For a positive control, 5 μl of diluted sample was mixed with 0.5 μl of denaturation buffer and incubated for 5 min at 37 °C. Then 1 μl of GlycoBuffer 2, 1 μl of NP-40 and 2.5 μl H_2O were added. After adding 1 μl of PNGase F, the reaction was incubated for 1 h at 37 °C. Prior to loading, all samples were incubated in loading buffer containing 12.5 mM DTT for 5 min at 37 °C. After SDS-PAGE, samples for orientation assay were processed as described under *Western Blot*.

3.5. SDS-PAGE

Diluted cell lysates and patch solutions were mixed with 2x loading dye containing 25 mM DTT. Followed by incubation for 5 min at 37 °C. Samples were loaded onto 10% polyacrylamide gel and run for 1.5 h at 130 V. 5 μg of total protein, as determined per BCA assay, were loaded per sample.

3.6. Western Blot

Proteins were transferred onto PVDF membrane using iBlot kit (P3, 11 min). Membranes were washed 1x with H_2O, and then incubated in 2% BSA in TBS + 0.1% TWEEN 20 (TBS-T) overnight at 4 °C. Membranes were rinsed 3 times for 5 min with TBS-T, followed by incubation with anti-PepT1 (Santa Cruz sc373742; mouse, 1:1000) antibody in 2% BSA/TBS-T for 1 h at room temperature. Membranes were rinsed 3 times for 5 min with TBS-T. Incubation with anti-mouse-HRP (rabbit, 1:1000) antibody in 2% BSA/TBS-T for 1 h at RT. Membranes were rinsed 3x 5 min with TBS-T. Blot was developed with ECL solution (1:1).

3.7. SSM-based electrophysiology.

Sensor preparation. In brief, SURFE^{2}R N1 1 mm or 3 mm single electrode sensors, or HTS SURFE^{2}R 96SE plates containing 96 sensor wells were thiolized with 1-octadecanethiol (0.5 mM in 2-propanol, 30 min), then dried and coated by adding 1.5 μl of 1,2-diphytanoyl-*sn*-

glycero-3-phosphocholine (DPhPC, 7.5 mg/ml in n-decane) and 50 µl of non-activating solution.

Adding the sample to the sensors. One aliquot of membrane vesicles was diluted 1:10 (single sensor) or 1:100 (HTS format) in non-activating solution, and briefly sonicated using a tip sonicator (UP 50H, Dr. Hielscher, equipped with MS 1 tip; 10 bursts, 20 % amplitude, 0.5 s cycle time). Then 10 µl of the vesicles were added to the SSM. This process is performed manually for N1 sensors by carefully submerging the pipette tip into the liquid. The 96SE sensor well plates are coated with lipid and PepT1 sample via an automated workflow. After the coating process, all sensors were centrifuged (1,000—2,000 g, room temperature, 30 min) before use.

Electrophysiological measurements on the SURFE^{2}R N1. The sensors were inserted into the measurement chamber. The integrated perfusion system automatically exchanged solutions using a fast switching 3-way valve and continuous flow at a flow rate of 200 µl/s. The currents were recorded in real-time using the Control Software v. 1.6.0.1. The order of solution flow is 1 s of non-activating (NA) solution, 1 s of activating (A) solution, 1 s of non-activating solution.

Electrophysiological measurements on the SURFE^{2}R 96SE. The sensor plate was inserted into the measurement chamber. Solution exchange takes place in a two step process: During the measurement a stack of 50 µl non-activating – 50 µl activating – 80 µl non-activating solutions are added at a flow rate of 200 µl/s from a pipette head loaded with 200 µl tips. After the measurement the liquid is removed from the sensor, leaving only ~ 30 µl behind, and the sensor washed twice with 200 µl non-activating solution to remove the substrate before starting a new measurement. The currents were recorded in real-time using the SURFControl Software.

More information on the basic procedure of SSME recordings both setups can be found in previous studies [22].

Solutions for electrophysiological measurements. Composition of non-activating solution (NA) and activating solution (A) differ for each assay. In general, solutions consisted of 25 mM Hepes, 25 mM MES, 140 mM KCl, 2 mM $MgCl_2$ and a particular concentration of substrate in A or glycine in NA.

During the typical H^+/substrate transport measurements, transport was initiated by exchanging glycine with an equal concentration of substrate (e.g. glycyl-glycine). In pH curves, pH was adjusted according to respective notion. Likewise, substrate concentration was adjusted during K_M measurements. Note that pH of every single final buffer (activating and non-activating) was and had to be controlled for, as substrates affect pH in a concentration-dependent manner. A pH difference between activating and non-activating buffer produces artifactual currents.

pH curve. pH curve was recorded using 20 mM glycine in the non-activating buffer, and 20 mM glycyl-glycine in the activating buffer. Sequentially, a given sensor was exposed to at least three solution exchange measurements for each pH.

Substrate affinity. Except for glycyl-glutamate the concentrations used were: 0.25 / 0.5 / 1 / 2.5 / 5 / 10 / 20 / 40 / 80 mM. Concentrations used for GlyGlu: 0.25 / 10 / 15 / 17.5 / 20 / 25 / 30 / 40 / 80 mM. Sequentially, a given sensor was exposed to at least three solution exchange measurements for each concentration. In ascending order, concentrations were increased.

Inhibitor studies. For all inhibitor studies 20 mM glycine in NA was exchanged against 20 mM glycyl-glycine in A. The first three measurements were performed in absence of inhibitor. A rinse with the respective inhibitor concentration in NA solution follows and the activation using 20 mM glycyl-glycine with inhibitor present in NA and A solution is repeated. In the single sensor format, rinsing and measurement are performed sequentially with increasing inhibitor concentrations on the same sensor. When using the 96SE, each sensor is treated with one inhibitor concentration and different inhibitor concentrations are applied to different sensors in parallel. The exact sequence of measurements is described in Fig. SI-5. The inhibitor concentrations are documented in Table 1.

3.8. Analysis of electrophysiological data

Capacitive currents were recorded using the SURFE^{2}R N1 Control Software and the SURFControl Software of the HTS instrument, respectively. Data was exported as ASCII files for subsequent analysis using Microsoft Excel and Origin 2019. In general, signal intensities were expressed via peak currents which served as representatives of the transport rate.

Data normalization and averaging. Peak intensities can vary from sensor to sensor. For data processing, (1) negative control currents are subtracted, (2) the set of traces recorded on a given sensor is normalized to the value obtained for a particular stimulus; i.e. pH 7.0 for GlyGly pH curve, highest substrate concentration for K_M, lowest specificity substrate for substrate comparison. Post normalization, (3) net values are averaged. For each data point, triplicates of at least 3 sensors were recorded. Errors are presented as the standard deviation of n experiments.

3.9. Theory/calculation

Time constants. Time constants are commonly employed to gauge the speed at which a system responds to a change, like how a transporter protein responds to substrate addition. The mono-exponential equation

Table 1
Inhibitor concentrations [mmol/L] used.

Single sensor format						
Zinc	Glibenclamide	Alafosalin	Lys[Z(NO2)]-Val	Valaciclovir		
	pH 6.7			pH 6.0	pH 6.7	pH 7.5
20	0.05	5	$5*10^{-3}$	5	5	5
6	0.01	1	$1*10^{-3}$	1	1	1
1.5	$2.5*10^{-3}$	0.25	$0.5*10^{-3}$	0.5	0.25	0.5
0.5	$0.5*10^{-3}$	0.05	$0.1*10^{-3}$	0.25	0.05	0.25
0.1		0.01	$0.01*10^{-3}$	0.125	0.01	0.125
				0.0625		0.0625
				0.01		0.01
HTS format						
Zinc	Valaciclovir	Glibenclamide				
	pH 6.7					
20	5	0.1				
6	1	0.04				
1.5	0.25	$12.5*10^{-3}$				
0.5	0.05	$2.5*10^{-3}$				

$$I(t) = A_1 * \exp\left(-\frac{t}{\tau}\right) + I_0 \quad (1)$$

served as a basis for calculation of the decay time, with peak current A_1, the time t, time constant τ, and baseline I_0. Rise time τ_1 is the time required to reach 63% of peak intensity. Decay time τ_2 is the time required for the trace to revert back to 37% of peak height. Averages of at least n = 3 sensors were taken for both 1 mm and 3 mm sensors. Likewise, correlation coefficients R were averaged.

pKa values. The Henderson-Hasselbalch equation forms the basis for acid-base chemistry, and pK values denote the pH at which protonation states tilt. Experimental pKa values were determined using Henderson-Hasselbalch-derived equations

$$\mathrm{I} = I_{max}/(1 + 10^{pKa-pH}), \quad (2)$$

for apparent acidic or

$$\mathrm{I} = I_{max}/(1 + 10^{pH-pKb}), \quad (3)$$

for apparent alkaline inactivation. For this purpose, the entire pH curve was cropped so that (a) only the ascending trend or (b) only the descending trend was fed into the equation. The value for pH 7.0 and 20 mM GlyGly was set as a normalizer (i.e. 1.0). As the experimental curve never exceeded a relative current of 1.2, this was set as $\mathrm{I_{max}}$ for I_{20mM} curves. No constraints were set for corrected curves.

Michaelis-Menten constant $\mathbf{K_M}$. The Michaelis-Menten constant $\mathrm{K_M}$ denotes the substrate concentration at which turnover is at half maximum capacity. The Hill equation models cooperative ligand binding to proteins [27]. If the Hill coefficient $\mathrm{n_{Hill}} > 1$, binding of one ligand enhances subsequent binding. If $\mathrm{n_{Hill}} < 1$, it reduces subsequent binding. At $\mathrm{n_{Hill}} = 1$, there's no cooperativity, and it follows Michaelis-Menten kinetics. Curves were fit using a Hill equation, i.e.

$$I = I_{max} * \frac{c^{n_{Hill}}}{\mathrm{K_M}^{n_{Hill}} + c^{n_{Hill}}} \quad (4)$$

with the substrate concentration c. The current I was taken as a proxy for the transport velocity V. Calculated maximum value (Imax) was set to 1.

Modelling of $\mathbf{K_M}$, pKa and $\widetilde{K}_S$-value. $\mathrm{K_M}$ as a function of pH, pKa and dissociation constant at saturated $\mathrm{H^+}$ concentration $\widetilde{K}_S$ for GlyGly had been modeled using an ordered binding model equation

$$\mathrm{K_M} = \widetilde{K}_S * (1 + 10^{pH-pKa}) \quad (5)$$

The fit was supplied with experimental $\mathrm{K_M}$ values.

Modeled $\mathbf{I_{max}}$. With modeled $\mathrm{K_M}$ values, corrected pH-dependent $\mathrm{I_{max}}$-values for GlyGly were calculated using experimentally obtained currents and the $\mathrm{K_M}$-based equation

$$I_{max} = \mathrm{I} * \frac{\mathrm{K_M(pH)} + [\mathrm{S}]}{[\mathrm{S}]}, \quad (6)$$

with substrate concentration [S] = 20 mM.

Substrate comparison: V_{max} and specificity. Responses for all nine substrates (80 mM) were recorded in parallel, i.e. on the same sensor. Measurement was performed on n = 3 sensors. Responses were normalized to the $\mathrm{I_{max}}$ of GlyGlu (arbitrarily, for the purpose of sorting by lowest specificity); i.e. for 80 mM of peptide *i*, the normalized current is

$$norm.\mathrm{I}_{80mM}(\mathrm{i}) = \frac{\mathrm{I}_{80mM}(\mathrm{i})}{\mathrm{I}_{max}(\mathrm{GlyGlu})} \quad (7)$$

Respective I_{max} values were obtained as described above in $\mathbf{K_M}$, and then normalized to $\mathrm{I_{max}}$(GlyGlu), i.e.

$$norm.\mathrm{I}_{max}(\mathrm{i}) = \frac{\mathrm{I}_{max}(\mathrm{i})}{\mathrm{I}_{max}(\mathrm{GlyGlu})} \quad (8)$$

Substrate specificity. Substrate specificity refers to the preference or selectivity of a protein for a particular substrate over others, and is particularly relevant for promiscuous proteins. Here, it was calculated by dividing Relative I_{max} by $\mathrm{K_M}$, i.e.

$$specificity = \frac{I_{max}}{\mathrm{K_M}}, \quad (9)$$

IC50. The IC50 value is a measure for an inhibitor's potency. It represents the concentration of an inhibitor required to reduce the transporter's activity by half in the presence of a substrate. Here, currents were induced by simultaneously adding 20 mM GlyGly and varying concentrations of the inhibitor. Curves were fit using the following equation:

$$I = I_{max} + \frac{(I_{min} - I_{max}) * c^{n_{Hill}}}{IC_{50}^{n_{Hill}} + c^{n_{Hill}}}, \quad (10)$$

with the inhibitor concentration c, the peak current at lowest inhibitor concentration I_{max} and peak at highest inhibitor concentration I_{min}, which was fixed to 0 in all fits to represent 'complete inhibition'. The Hill coefficient in this scenario would point out cooperativity for subsequent inhibitor binding or decreased affinity for the substrate.

4. Results

4.1. hPepT1 elicits currents in SSME

Membrane vesicles were produced from hPepT1-overexpressing CHO cells. The schematic in Fig. 1A shows the process of membrane vesicle preparation; in brief, cells are disrupted by nitrogen decompression and membranes are separated along a sucrose gradient. Fractions F1 and F2 are collected from the interfaces between 9% and 31% sucrose or 31% and 45% sucrose, respectively. Western Blot (WB) analysis of whole cell lysates and membrane vesicles from hPepT1(+) CHO cells confirmed the presence of the transporter in both fractions. For electrophysiological analysis the enrichment of hPepT1 in the F1 band was used. As a negative control, vesicles obtained from non-overexpressing CHO cells (fraction F) were used for the blot, as well as in all subsequent electrophysiological measurements. The results of the WB are discussed in further detail in SI-1. In addition, we used dynamic light scattering to determine the vesicles sizes, which averaged around 230–280 nm, and we investigated the transporter orientation in the vesicles via a glycodigest assay (SI-1, and Fig. SI-1). We found predominantly right-side-out orientation for F1 as one would expect under physiological conditions, which is important for further interpretation of kinetic parameters. This means the kinetic data obtained from our in vitro studies correspond to H+/peptide influx into the cell. For electrophysiological characterization, purified vesicles are added to a sensor. The instrument performs a fast solution exchange above the sensor surface, providing the peptide substrate at a defined pH to activate hPepT1. A current trace is recorded in real-time. A schematic including a representative trace of a transport current elicited by hPepT1 (+) membrane vesicles is shown in Fig. 1B, along with a current recorded with the control. To determine the hPepT1-related transport current during data analysis, signals from control membranes were always subtracted. The cartoon below correlates to the current trace. At t = 1.1 s, the non-activating (NA) solution that does not contain any peptide is exchanged above the sensor surface for the activating (A) solution that contains the peptide substrate, resulting in a steep current rise. The A solution holds 20 mM GlyGly as activating substrate, while the NA solution provides same amounts of glycine, which does not interact with hPepT1. The pH was set to 7.25. The positive capacitive current indicates $\mathrm{H^+}$-coupled, inward-directed transport of GlyGly, which generates a positive membrane voltage. The transport follows an electrochemical gradient given by the GlyGly concentration gradient.

The current returns to the baseline when voltage generated by $\mathrm{H^+}$ translocation blocks any further influx (electrochemical equilibrium). At t = 2.1 s, A solution is exchanged for NA solution; $\mathrm{H^+}$/GlyGly efflux is observed as a negative capacitive current. When the current reaches the

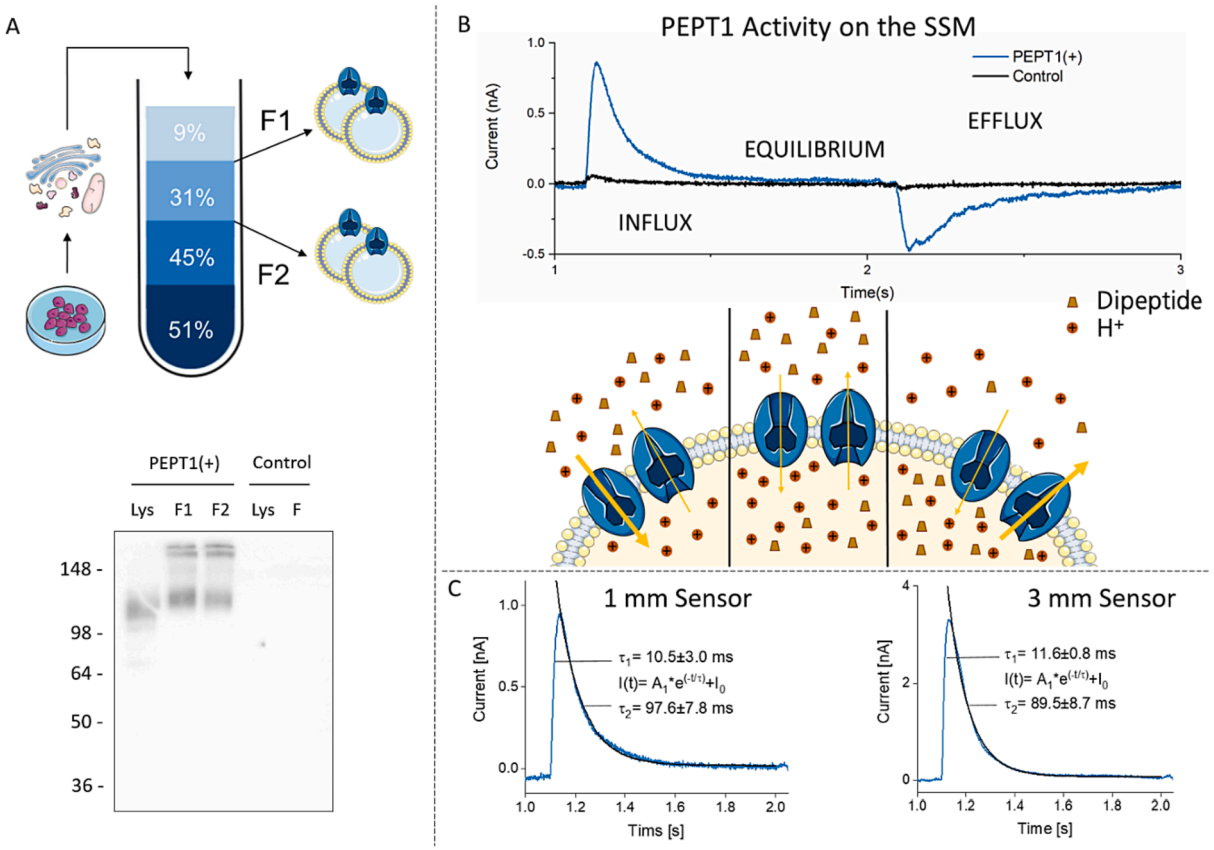

Fig. 1. Sample preparation and validation of the electrophysiological assay. (A): Schematic illustrating the production of membrane vesicles (top) according to the description in Experimental Section, and Western Blot of lysates and vesicles (bottom). Lys, cell lysate; F1, upper hPepT1(+)-fraction harvested from sucrose gradient (interface 9/31%); F2, lower hPepT1(+)-fraction harvested from sucrose gradient (interface 31/45%); F, lower PepT1(-)control-fraction harvested from sucrose gradient (interface 31/45%). 5 μg total protein were loaded. (B): Representative SSME traces for hPepT1 (blue) vs control (black) membranes and schematic of the substrate fluxes in the corresponding phases. Influx is triggered ~ 1.1 s after initiation of one NA-A-NA measurement cycle; in the beginning [0;1 s] the sensor is rinsed with NA solution (not shown); followed by an exchange with activation solution A [1;2 s], that reaches the sensor surface at ~ 1.1 s. H^+/peptide coupled influx takes place until an electrochemical equilibrium is attained. The influx of positive charge is reflected by a positive capacitive current. Finally, buffer conditions are reverted to non-activating conditions applying NA solution [2;3 s]; The substrate moves out of the vesicles, resulting in a negative capacitive current. (C): Time constants for 20 mM GlyGly at pH 7.25 using 1 mm sensors (left) or 3 mm sensors (right). Current traces were taken from one representative sensor (blue). Time constants τ_1 and τ_2 were derived from mono-exponential fits. Decay fits are highlighted (black). Values reflect averaged values from n = 3 sensors each, with R^2(1 mm) ≥ 0.984 and R^2(3 mm) ≥ 0.990; τ_1, rise time; τ_2, decay time. (For interpretation of the references to colour in this figure legend, the reader is referred to the web version of this article.)

baseline, initial conditions are restored and another solution exchange experiment may be performed. The peak current amplitude is used as a measure for transport activity. Note that in SSME, voltage is not controlled directly, and dV across the membrane is around zero in this setup when transport is initiated. This is a key difference to other setups like TEVC, where the clamped voltage of the living cells plasma membrane may influence the kinetic parameters of the transporter.

4.2. Addition of substrate evokes transport currents only

All currents recorded using SSME are transient due to the capacitive read-out, including transport currents that would be measured as steady-state currents in conventional electrophysiology [22]. Pre-steady-state (PSS) currents which occur for hPepT1 in conventional electrophysiology are thought to be a product of reorientation of the empty carrier and binding/dissociation of H^+ [28,29]. The empty carrier contains the negatively charged proton binding site, which is translocated from inward to outward facing after intravesicular H^+-dissociation, and applied voltage steps in conventional electrophysiology do directly trigger this voltage dependent step of the transport cycle.

In SSME, we used peptide concentration jumps to elicit transport. Substrate concentration jumps may also trigger electrogenic PSS events, such as fast substrate-induced conformational transitions that are not easily distinguishable from transport currents in SSME recordings. Therefore, the first step in SSME experiments is to validate the type of current that is detected to ensure proper data interpretation. When fast PSS currents occur, they overlay with the transport current, thus two components of different kinetics create the signal, likely leading to a bi-exponential decay. We compared the traces obtained from 3 mm sensors (high signal intensity, low time resolution) versus 1 mm sensors (lower signal intensity, strong time resolution). We do not visually infer PSS currents for hPepT1, and observe a mono-exponential decay, and the time constants obtained from mono-exponential fits of the current rise and decay are essentially the same for 3 mm and 1 mm sensors (Fig. 1C). Thus, we do not detect any peptide-binding related PSS currents. Therefore, any peptide-induced signals in hPepT1 vesicles may be attributed to transport events, allowing the derivation of transport V_{max} values from peptide-induced concentration dependent peak currents, and the conclusion of K_M values from hyperbolic Hill fits (note that all formulas and fits are found under Theory/calculations).

4.3. Transport currents in hPepT1 are pH-dependent

Peptide translocation mediated by hPepT1 is strictly coupled to protons [30]. In order to investigate the pH dependence of hPepT1, we triggered transport with 20 mM GlyGly at different pH values. We investigated a pH range from 5.0 to 9.0 and found a bell-shaped activity curve (Fig. 2A). Representative current traces for hPepT1(+) vesicles for the ascending trend (Fig. 2B) and the descending trend (Fig. 2C) are shown. Comparisons to negative controls are shown Fig. SI-2. Due to variations between sensors, peak currents are normalized before averaging across multiple experiments. Here, peak currents were normalized to the peak current recorded at pH 7.0 for each sensor, then all normalized peak currents were averaged across sensors. Henderson-Hasselbalch fits for apparent acidic (Fig. 2D) and alkaline (Fig. 2E) inactivation yield two apparent pK values of pKa = 6.45 and pKb = 8.11, respectively.

We investigated the peptide concentration dependence at different pH values to elucidate whether K_M values for GlyGly are pH-dependent. We used GlyGly concentrations between 0.1 mM and 80 mM (Fig. 3A).

K_M values steeply increase with pH, ranging from 1.64 at pH 6.0 to 50.07 mM at pH 8.0. Using the pH-dependent K_M values and a model equation based on ordered substrate binding, we derived the apparent substrate affinity $\widetilde{K}_S$ under saturating H^+ concentration of 1.42 mM and an apparent pKb of PepT1 of 6.35 (Fig. 3B). This pKb represents proton binding to the outward facing carrier, which affects the affinity of PepT1 for the peptide. The graphical inlet highlights the effect of proton depletion onto the initial steps of the transport cycle, i.e. protonation, and substrate binding of the carrier. Assuming that pH-dependent changes in K_M for the peptide do reflect changes in peptide affinity (K_D), the pKb value can be determined via the pH-dependent K_M values. The acquired value of 6.35 will be further discussed below.

The pH-dependent K_M values were then used to correct the experimentally derived pH curve in order to reflect pH-dependent I_{max} values (Fig. 3C).

The curve shows a broader plateau, and corrected maximum transport rates even increase at more alkaline pH.

To examine the impact of the pH-dependent apparent affinity on the pKa determined from the acidic downregulation (Fig. 2D), a Henderson-Hasselbalch fit was used to conclude a corrected pKa value from the corrected pH curve. The corrected pKa value of 7.09 is only slightly higher than the value of 6.45 determined from the original data (Fig. 3C). This is expected since the GlyGly concentration used to measure the pH activity curve (20 mM) is close to – albeit not exactly at – saturation for the whole pH-range of acidic downregulation (compare Fig. 2 and Fig. 3).

4.4. Substrate comparison

All measurements shown above used GlyGly as a substrate. Yet, the range of potential hPepT1 substrates is broad, and knowledge about apparent affinity (K_M) and transport capacity (I_{max}) for different peptide substrates helps to understand the basis of substrate-transporter interactions, and consequently in drug design. To compare and quantify substrate specificity, usually V_{max}/K_M ratio is used as a measure; the higher the value, the higher the specificity for a given substrate. We showed above that we can conclude K_M values from concentration dependent peak currents because the recorded currents reflect steady-state transport only.

Naturally, the substrate composition (including the order within a pair of amino acids) affects the apparent affinity (K_M) due to different rates for peptide binding; and due to different *translocation rates* resulting from different energy barriers for the conformational transitions that move the different peptide/transporter complexes across the membrane. We sought to test various substrates to learn more about the implications of steric and charge-related features of substrate moieties on peptide translocation kinetics. For this, we used several Gly-X peptides (X being a placeholder for the C-terminus), and determined K_M and relative I_{max} values. We determined K_M values from peptide concentration sequences measured on the same sensor (Fig. 4A). In order to compare relative I_{max} values across substrates and to neglect variations between sensors, we also applied all nine substrates at 80 mM on the same sensor (Fig. 4B), and used the relative currents for normalization of

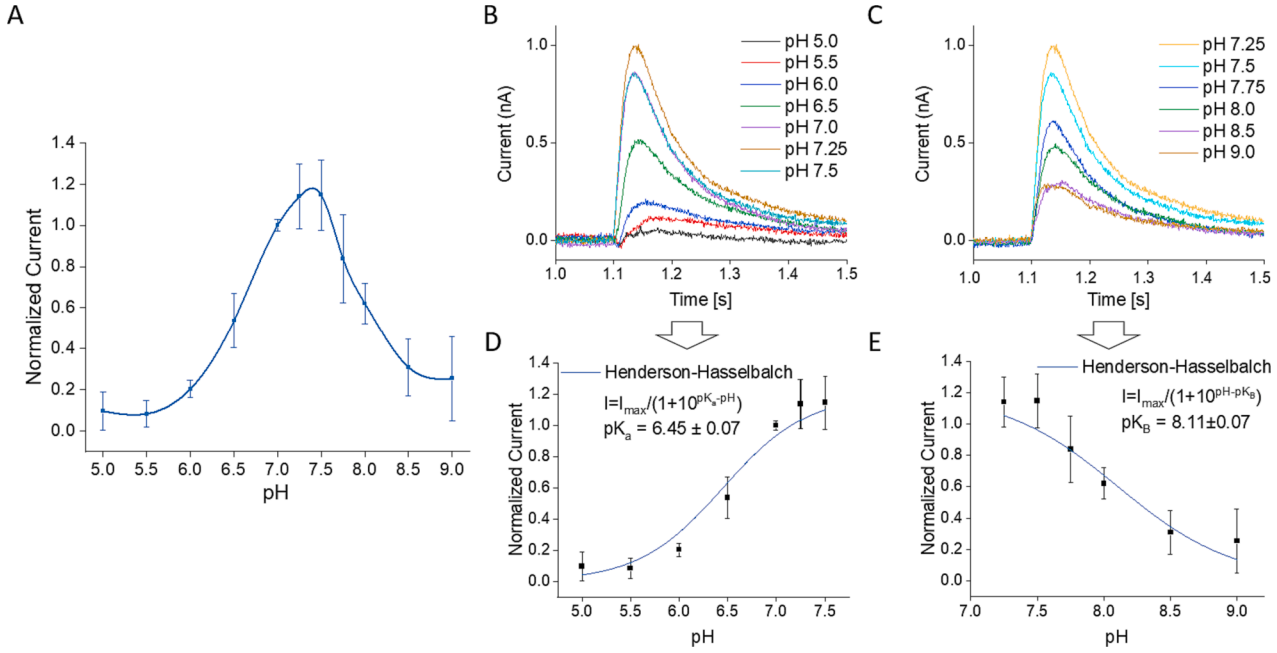

Fig. 2. H^+/GlyGly cotransport rate as a function of pH using 20 mM GlyGly. (A): Normalized peak currents over a pH range from 5.0 to 9.0. Negative control values were subtracted and activity was normalized relative to peak currents at pH 7.0. (B): Representative transport currents for hPepT1(+) vesicles over a pH range from 5.0 to 7.5. (C): Representative transport currents for hPepT1(+) vesicles over a pH range from 7.25 to 9.0. (D): Ascending curve for acidic inactivation with Henderson-Hasselbalch fit and resulting pKa = 6.45 ± 0.07. (E): Descending curve for alkaline inactivation with Henderson-Hasselbalch fit and resulting pKb = 8.11 ± 0.07. N = 4 sensors for pH 7.25 and 7.75, and N = 7 sensors for all other pH-values. Error bars represent standard deviations.

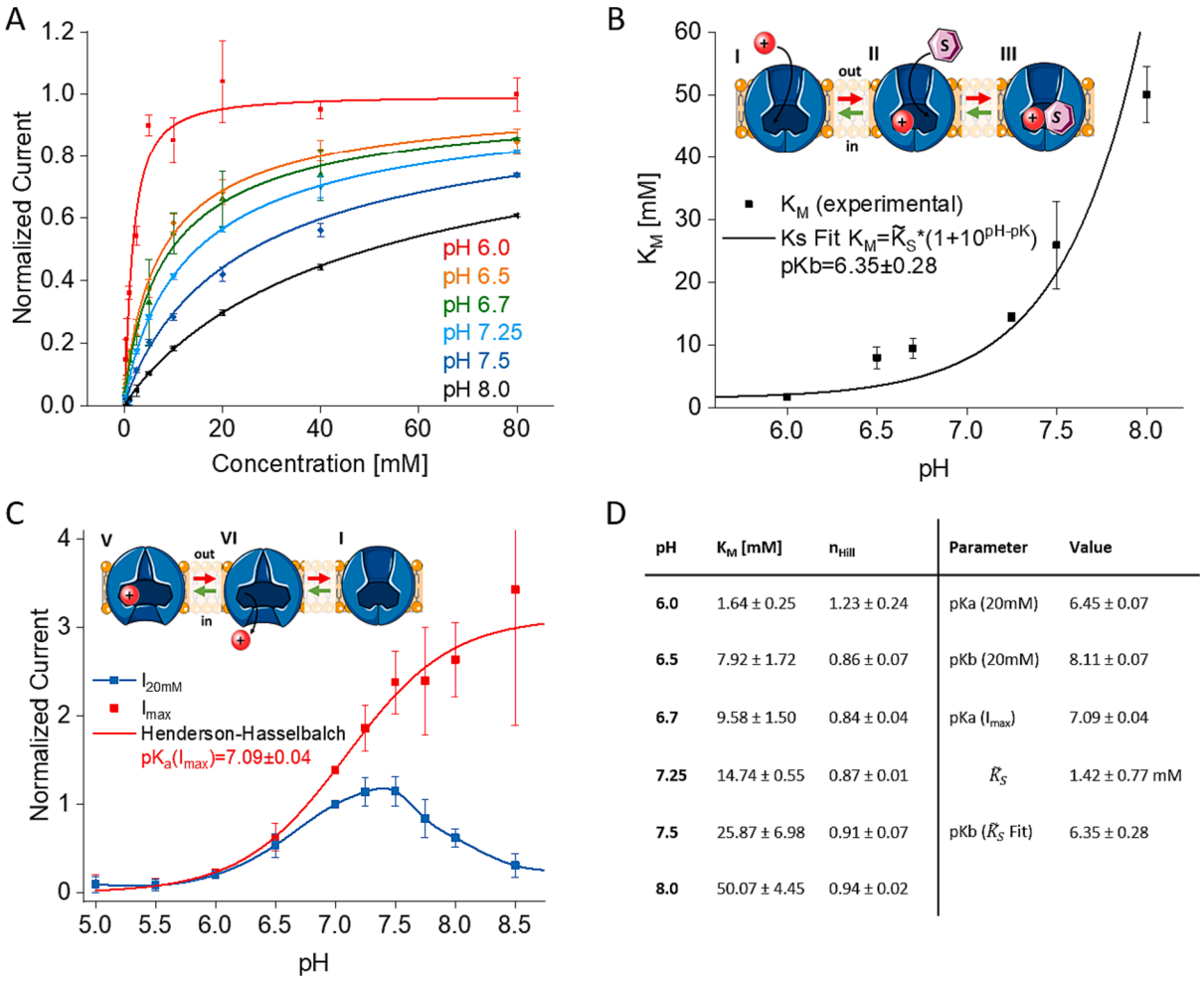

pH	K_M [mM]	n_{Hill}	Parameter	Value
6.0	1.64 ± 0.25	1.23 ± 0.24	pKa (20mM)	6.45 ± 0.07
6.5	7.92 ± 1.72	0.86 ± 0.07	pKb (20mM)	8.11 ± 0.07
6.7	9.58 ± 1.50	0.84 ± 0.04	pKa (I_{max})	7.09 ± 0.04
7.25	14.74 ± 0.55	0.87 ± 0.01	$\tilde{K}_S$	1.42 ± 0.77 mM
7.5	25.87 ± 6.98	0.91 ± 0.07	pKb ($\tilde{K}_S$ Fit)	6.35 ± 0.28
8.0	50.07 ± 4.45	0.94 ± 0.02		

Fig. 3. Impact of pH on apparent substrate affinity. (A): Dose response curves for GlyGly at various pH values. Concentration dependent peak currents obtained for a given sensor were fitted using a Hill equation, normalized to respective I_{max} and then averaged across sensors. Three measurements were performed per sensor per concentration with N ≥ 3 sensors, negative control values were subtracted. (B): K_M values for GlyGly were plotted over pH. Apparent substrate affinity at saturating H^+ concentration $\tilde{K}_S = 1.42 \pm 0.77$ mM was derived using a model equation (see Experimental); a modeled curve for K_M as a function of pH was obtained. The built-in schematic highlights the steps which primarily affect the K_M, i.e. proton and substrate binding. (C): Modeled K_M-values were fed into a K_M equation to correct experimental normalized currents, and to attain theoretical maximum signals (I_{max}) assuming substrate saturation. Modeled data (red) and experimental data (blue) are shown. For all plots, error bars represent standard deviations. The built-in schematic highlights the steps which primarily affect I_{max}, i.e. proton release and return of the empty carrier. (D): Summary of acquired parameters. (For interpretation of the references to colour in this figure legend, the reader is referred to the web version of this article.)

the concentration dependent datasets. A pH of 7.25 was chosen, as it represented the pH optimum for GlyGly. The same sets of concentrations were used for most substrates, except for GlyGlu (see figure description).

Here, intermediate concentrations were increased due to the high K_M. Representative current traces, respective signals elicited from control membranes and the hyperbolic fits of the peak currents are displayed in Fig. SI-3 and SI-4. Notably, the peptides GlyGlu, GlyAsp and GlyPhe generated background currents on the negative control (Fig. SI-4), introducing degrees of uncertainty which are reflected in the error bars (Fig. 4). This is not surprising given that hydrophobic compounds or such containing benzene rings intercalate into the membrane and compounds carrying a net charge bind to the hydrophilic surface of the membrane, both generating capacitive currents, typically described as artifacts [22]. However, it's intriguing that GlyTyr, despite having a benzene ring, did not produce such artifacts. This might be attributed to the hydroxyl group of Tyr making it slightly less hydrophobic than Phe [31], and potentially keeping it from invading the membrane.

We have identified a 23-fold difference in apparent affinities across all tested peptides in the following order (Fig. 4A): GlyPhe (1.93 mM) < GlyVal (3.89 mM) < GlyGln (4.35 mM) < GlyTyr (5.04 mM) < GlyGlyGly (8.52 mM) < GlyGly (14.74 mM) < GlySar (23.99 mM) < GlyAsp (24.17 mM) < GlyGlu (44.86 mM). Relative I_{max} values on the other hand varied only ~ 2.6-fold in the ascending order of GlyGlu < GlyTyr < GlyGln < GlyAsp < GlyVal < GlyPhe < GlyGlyGly < GlyGly < GlySar (Fig. 4B).

Finally, we calculated substrate specificities (I_{max}/K_M) normalized to GlyGlu. Substrate specificity differs by a factor of 45 across all tested peptides and increases in the following order: GlyGlu < GlyAsp < GlySar < GlyGly < GlyGlyGly < GlyTyr < GlyGln < GlyVal < GlyPhe (Fig. 4C & D), essentially the same order as reported for the apparent affinities.

4.5. *Inhibitor studies using SSME in a high throughput format*

We developed an inhibitor assay to study the inhibition of hPepT1-mediated H^+/GlyGly transport using various inhibitors (Fig. 5). We tested five compounds that were described to inhibit hPepT1-mediated H+/GlyGly transport to validate our approach.

Inhibitor assays using SSME are performed in a 2-step experiment: On a given sensor, first 20 mM GlyGly is used to record the reference

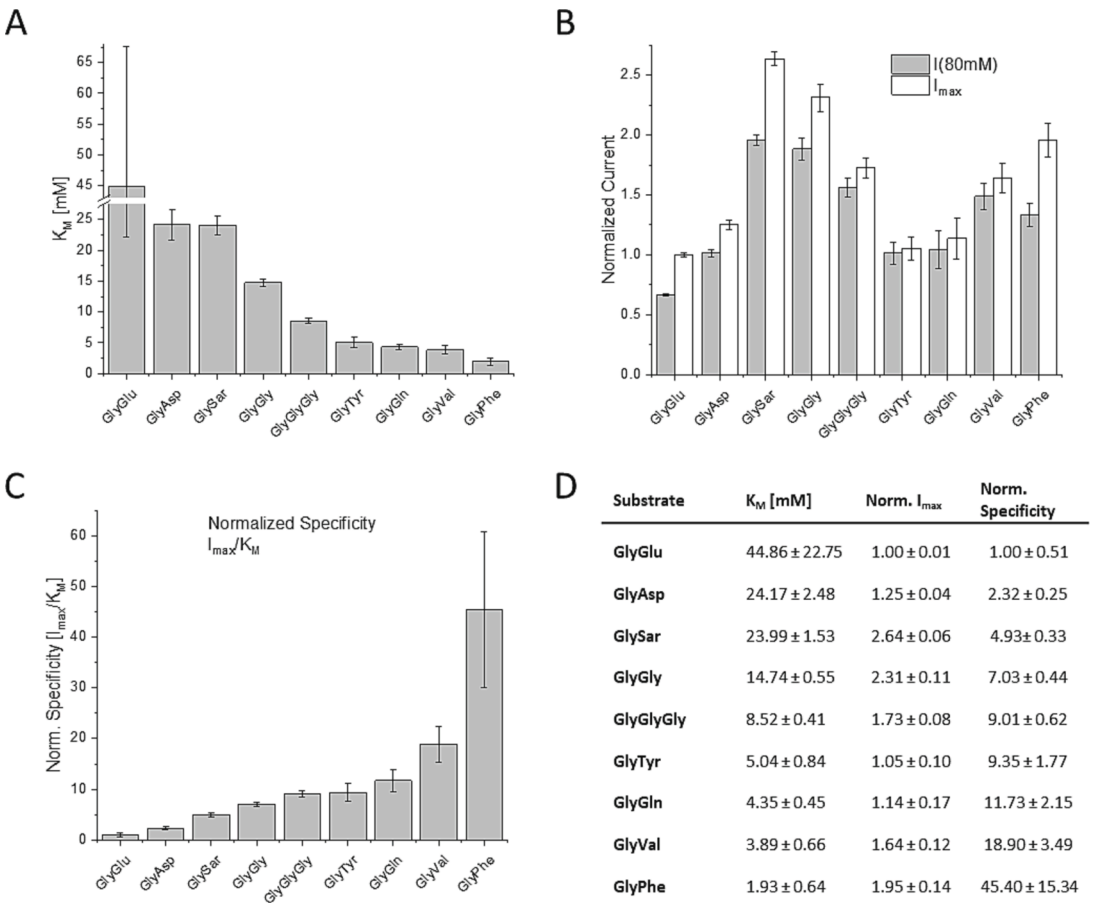

Substrate	K_M [mM]	Norm. I_{max}	Norm. Specificity
GlyGlu	44.86 ± 22.75	1.00 ± 0.01	1.00 ± 0.51
GlyAsp	24.17 ± 2.48	1.25 ± 0.04	2.32 ± 0.25
GlySar	23.99 ± 1.53	2.64 ± 0.06	4.93± 0.33
GlyGly	14.74 ± 0.55	2.31 ± 0.11	7.03 ± 0.44
GlyGlyGly	8.52 ± 0.41	1.73 ± 0.08	9.01 ± 0.62
GlyTyr	5.04 ± 0.84	1.05 ± 0.10	9.35 ± 1.77
GlyGln	4.35 ± 0.45	1.14 ± 0.17	11.73 ± 2.15
GlyVal	3.89 ± 0.66	1.64 ± 0.12	18.90 ± 3.49
GlyPhe	1.93 ± 0.64	1.95 ± 0.14	45.40 ± 15.34

Fig. 4. Comparison of apparent substrate affinities, relative I_{max} values and specificities at pH 7.25. (A): Apparent substrate affinities. K_M values were determined for GlyGly, GlyGlyGly, GlySar, GlyGlu, GlyGln, GlyAsp, GlyVal, GlyTyr, and GlyPhe. (B): Differential peak currents as a function of substrate, normalized to I_{max} of GlyGlu. Peak intensities were compared for 80 mM of substrate (grey); additionally, the calculated I_{max} (white) is shown. (C): Substrate specificities expressed as I_{max}/K_M, normalized to I_{max} of GlyGlu. Three measurements were performed per sensor per concentration and substrate with N = 3 sensors. Error bars represent standard deviations. (D): Summary of peptide dependent kinetic parameters.

peak current (I_{ref}) in absence of inhibitor; second, the inhibitor is added to both, non-activating and activating solutions and the 20 mM GlyGly concentration jump is repeated to measure a reduced peak current I; The % of inhibition may be obtained by calculating the ratio I/I_{ref}.

When determining IC_{50} values, increasing inhibitor concentrations are used sequentially on the same sensor. Using n = 3 sensors for each inhibitor and a pH of 6.7, we determined IC_{50} values of 0.68 μM for Lys[Z(NO_2)]-Val, 50 μM for Glibenclamide, 419 μM for Valaciclovir, 1.2 mM for Alafosalin, and 6.0 mM for Zinc (Fig. 5A). These values are mostly consistent with literature values that are 2 μM, 25 μM, 460 μM, 190 μM, and 3.4 mM, for these compounds, respectively [32–36]. Largest deviations were shown for Lys[Z(NO_2)]-Val which was 3 times more potent in our assay and Alafosalin, which was 6 times less potent compared to literature values. Small variations in IC_{50} values may have their origin in different assay conditions, i.e. substrate concentrations, voltage, cell-type etc.

We saw before that an increasing pH reduces the apparent substrate affinity (Fig. 3), which might be also relevant for inhibitors, depending on their mechanism of action. To put this to the test, we recorded IC_{50} curves for Valaciclovir at different pH values. We selected Valaciclovir because it was described to act as a competitive inhibitor, binding to the same site as GlyGly [37–40]. Therefore, it may also only bind to the protonated carrier. We determined IC_{50} values of 380 μM, 419 μM, and 1.2 mM at pH 6.0, 6.7, and 7.5, respectively (Fig. 5B). The pH relationship of these values is pointing in the same direction as for GlyGly, indicating that this inhibitor also predominantly binds to protonated PepT1. However, the relationship is less extensive (compare K_M value development from pH 6.0 to 6.7, Fig. 3D).

We then transferred the inhibitor assay from the single sensor to the high throughput format, enabling the recording of 10.000 data points per day and the screening of compounds in a 96 sensor well-plate format. In brief, 96 sensors are recorded in parallel by injecting stacked non-activating and activating solutions from a pipette head containing 200 μl pipettes [22]. Parallelization enables different assay designs. We chose to determine IC_{50} values of three inhibitors using four inhibitor concentrations each, allowing for n = 8 repetitions in parallel. IC_{50} curves for Glibenclamide, Valaciclovir and Zinc are shown in Fig. 5C. An overview of all determined IC_{50} values are given in Fig. 5D, which shows that IC_{50} values determined with the two different platforms do match very well, even though a different number of data points and different concentration ranges are used for the experiments, indicating straight-forward assay transferability across those platforms.

The layout of the 96 sensor well-plate used for the HTS inhibitor experiment is shown in Fig. 5E. Each column of the sensor plate was used to add a different inhibitor concentration. Parallelization required in-well normalization in order to determine IC_{50} values. Hence, each well was used for the measurement in absence of inhibitor. The measurement in presence of inhibitor was then normalized to this value. The sequence of measurements is further layed out in Fig. SI-5. Fig. 5F shows representative current traces recorded in the 96 sensor well-plate format. The green trace represents a recording post washout, highlighting reversibility of inhibition. Of note, washout tests were not conducted for all compounds. We anticipate that not all of them will be easily washed out; the more hydrophobic ones, in particular, may present challenges.

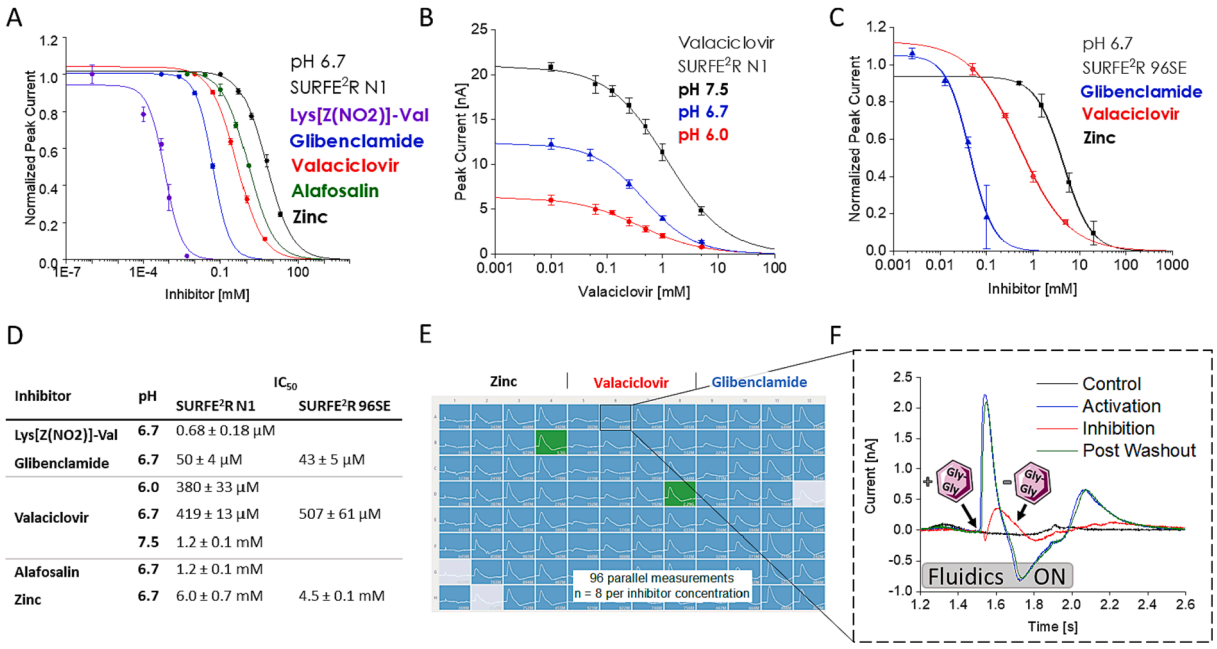

Inhibitor	pH	IC_{50} SURFE²R N1	IC_{50} SURFE²R 96SE
Lys[Z(NO2)]-Val	6.7	0.68 ± 0.18 µM	
Glibenclamide	6.7	50 ± 4 µM	43 ± 5 µM
Valaciclovir	6.0	380 ± 33 µM	
	6.7	419 ± 13 µM	507 ± 61 µM
	7.5	1.2 ± 0.1 mM	
Alafosalin	6.7	1.2 ± 0.1 mM	
Zinc	6.7	6.0 ± 0.7 mM	4.5 ± 0.1 mM

Fig. 5. Inhibitor studies using 3 mm SURFE²R N1 sensors (A-B) and HTS 96 sensor well plates (C, E, F). All determined IC_{50} values are summarized in (D). Experiments were carried out using 20 mM GlyGly in all A solutions. (A): IC_{50} curves for hPepT1 inhibitors measured at pH 6.7. Each inhibitor was measured at a different sensor and datasets were normalized to the current response in absence of inhibitor, followed by averaging across sensors. Average and standard deviation across N = 3 sensors are shown. (B): IC_{50} curves for Valaciclovir at pH 6.0, pH 6.7, and pH 7.5. Each pH was measured at a different sensor. Average and standard deviation across n = 3 sensors are shown. (C): IC_{50} curves for hPepT1 inhibitors measured in HTS format. All measurements were performed on the same sensor well plate (compare E). Each inhibitor concentration was recorded on N = 8 individual sensors. Peak currents were normalized to the peak current recorded in absence of inhibitor on the same well, then averaged across sensors. (D): Overview about all recorded IC_{50} values. The IC_{50} values obtained with the single sensor format and the HTS are very similar, supporting assay transferability. (E): Screenshot of the SurfControl Software showing the 6th measurement for each sensor well, that resembles the second measurement after application of inhibitor. The complete sequence of measurements is indicated in Fig. SI-5. Inhibitors are indicated and concentrations decrease from left to right per column of the 96 sensor well plate. (F): Recorded current traces for the sequential measurements using the representative sensor well A6. The time of solution application is indicated in grey (Fluidics ON), and time points for substrate (GlyGly) addition and removal are indicated. The peak current after GlyGly addition is used for analysis. Control (black), no substrate; Activation (blue), 20 mM GlyGly; Inhibition (red), 20 mM GlyGly + inhibitor; Post-Washout (green), regenerated signal (20 mM GlyGly) after inhibitor washout. Inhibitor concentrations are documented in Table 1. (For interpretation of the references to colour in this figure legend, the reader is referred to the web version of this article.)

5. Discussion

For our investigations, we produced hPepT1-containing vesicles from overexpressing cells (Fig. 1A), added them onto a solid supported membrane and measured substrate-elicited responses in the form of capacitive currents (Fig. 1B).

We analyzed the current traces for PSS currents. Those are typically more prominent on 1 mm sensors due to their higher time resolution, leading to altered time constants for the current rise and/or decay. Substrate binding induced PSS currents from SSME recordings have been recently discussed for the H^+/sugar cotransporter XylE and for the Na^+/sugar cotransporter SGLT1 [19,20,41].

The lack of PSS currents (Fig. 1C) allowed us to treat peak currents as a read-out for the transport current.

5.1. Transport currents in hPepT1 are pH-dependent

We studied the pH dependence of GlyGly transport via hPepT1. For 20 mM substrate, we found two pKa values, namely pKa = 6.45 and pKb = 8.11. Both match decently well to previously attained values for conditions without pH gradients, i.e. with same pH values at both sides of the membrane [42], as is the case in our SSME experiments. The reduced transport rate at acidic pH is likely due to a shift in equilibrium of the intravesicular H^+ release step, which affects the rate of the empty carrier translocation, as proposed before for H^+-coupled sugar transporters [43]. The acidic pKa likely reflects the deprotonation step of H57 in the inward facing carrier with direct impact on the maximum transport rate (V_{max}) [44].

We suspected, the reduced transport rate at alkaline pH may be attributed to one of two reasons. Either the binding of H^+ to the outward-facing carrier modulates the rate-limiting step of H^+/peptide cotransport, i.e., the *alternating access* of the substrate-bound carrier. This would result in a reduction of V_{max} when protons are depleted. Alternatively, the reduction of H^+-bound hPepT1 at alkaline pH leads to a lower *apparent affinity* for the peptide, resulting in a reduced transport rate due to undersaturation of the peptide binding site.

5.2. The external pH affects apparent substrate affinity

To find the reason of alkaline downregulation, we determined K_M as a function of pH, and found a steep K_M increase in the alkaline (Fig. 3B). Thus, the substrate concentration of 20 mM used to generate the pH curve (Fig. 2B) was saturating for acidic conditions (the detected currents were close to I_{max}), whereas 20 mM was non-saturating and even below K_M for pH ≥ 7.5. Hence, the pKb of 8.11 derived from the bell-shaped curve (Fig. 2A) can be assumed to be a direct consequence of undersaturation, and does not reflect an inherent property of the transporter. Thus, proton depletion has no direct impact on I_{max}, as was observed for H^+- coupled sugar transporters [43].

The model equation based on ordered substrate binding ($\widetilde{K}_S$-fit) yields a pKb of 6.35, which is in agreement with previous reports, indicating that extracellular pH levels below 6 are required for optimal function of PepT1 [45].

As the model focuses on substrate interactions, rather than on maximum turnover, we conclude that H^+- binding (reflected by pkb) predominantly affects the apparent affinity for the peptide. This implies

a strict binding order, i.e. the H^+ binds first.

On a side note, the pH-dependent K_M values and the determined pKb cannot be attributed to a reduction of effective GlyGly concentration. In the tested pH range between pH 5.0 and pH 8.0, GlyGly is predominantly in its zwitterionic state, in which it is transported, since pK values of the amino- and carboxy-termini are 3.1 and 8.1, respectively [46,47].

5.3. The internal pH affects I_{max}

Using a K_M-based equation, we corrected the experimental pH curve, and reapplied the Henderson-Hasselbalch fit. The determined pKa value of 7.09 presents the H^+ release step in the inward facing conformation. Internal acidification below pH ~ 7.5 impairs the H^+ release of the inward-facing carrier (Fig. 3C), affecting the rate of the following conformational transition of the empty carrier, which limits the overall velocity of H^+/peptide cotransport. This supports the common notion that the transition of the carrier, in particular the return of the empty carrier is rate limiting [6,48,49]. Fittingly, data obtained for zfPepT1 show a faster cycle completion in the alkaline, attributed to increased transitional rates [50].

5.4. Physiological pH conditions drive peptide transport

Interestingly, the pK values for proton binding and proton release which impact the peptides K_M and I_{max} of the transport - are quite similar, with pKb = 6.35 and pKa = 7.09, respectively. So, the protonation steps of the transport cycle in hPepT1 display a high degree of symmetry. How does that project towards facilitating directed transport at physiological pH?

Considering a well-regulated intracellular pH between 7.0 and 7.4 [51], transport I_{max} is almost at its peak, since the pKa for proton release is mostly below intracellular pH. PepT1 is expressed in enterocytes of the small intestine with extracellular pH levels gradually increasing from pH 6.0 to pH 7.4 [52]. Since proton binding with pKb = 6.35 affects the apparent affinity for the peptide, transport rates at a given peptide concentration are higher in the upper region of the small intestine. Since both, apparent affinity for the peptide and the available peptide concentrations will decrease along the small intestine, peptide adsorption via PepT1 may not be relevant in the lower regions.

We conclude that the natural pH gradient across the plasma membrane of enterocytes is important to drive H^+/peptide transport in hPepT1. However, in contrast to channels where the ion gradient directly drives ion translocation, the relevant parameters are the dissociation constants (here: pK values) in the inward and outward facing conformation and the resulting binding equilibria that affect other kinetic parameters, such as I_{max} and the apparent affinity (K_M) for the co-substrates.

5.5. Substrate specificity is determined by apparent affinity

We studied the transport of several substrates with varying C-termini (Fig. 4).

Comparing substrate affinities (Fig. 4A), we conclude that hydrophobic C-terminal residues increase apparent affinity, while charged C-terminal residues decrease apparent affinity. The order in apparent affinity based on the C-termini (Phe > Val > Gln > Tyr > GlyGly / Gly / Sar > Asp > Glu) was similar as reported for yeast Ptr2p (Phe > Tyr > Val > Gln > Gly > Glu > Asp) [53]. Likewise, greater hydrophobicity was shown to be correlated with higher apparent affinity in bPepT1 [54], but contrary to our results similar observations were made for negatively and neutrally charged substrates.

In contrast to K_M, I_{max} was mostly unaffected by the type of peptide (Fig. 4), showing only a 2.6-fold variation across all tested substrates. We can consider that K_M is an indicator of peptide-specific binding and transition events, whereas I_{max} reflects the rate limitation of the entire transport cycle, which is the translocation of the empty carrier. The observed lack of correlation between K_M and I_{max} for different peptides confirms that they have distinct molecular origins.

We then calculated the specificities (I_{max}/K_M, Fig. 4C), and found that they were mostly defined by K_M which maps well onto previous TEVC results [55]. Thus, the rate constants of conformational transitions within the peptide bound carrier are affected by the type of peptide, as K_M is a consequence of the sum of rates of all individual reaction steps [56]. However, the fact that I_{max} is only slightly affected by the type of peptide insinuates that not binding nor translocation of the peptide, but rather deprotonation and / or the return of the empty carrier represent the major rate-limiting steps for the transport.

5.6. A kinetic model for H^+/peptide cotransport in hPepT1

Considering the reported pH and substrate dependencies, we conclude and discuss some mechanistic insights about the transport cycle that we integrated into a schematic (Scheme 1). We found that H^+ depletion (alkaline pH) reduces the apparent affinity for the peptide (Fig. 3B), indicating a strict binding order in agreement with the literature: the proton binds first [29,44,55,57–59], followed by substrate binding (Schematic 1, steps I, II to III) which is thought to rely on the carboxy and amino termini of the substrates being recognized by conserved basic and acidic side chains within the highly charged dipolar binding site of the transporter [1,60]. In addition, we could not detect a reduction in I_{max} upon H^+ depletion (Fig. 3), indicating that substrate binding and the subsequent alternating access of the loaded carrier are not rate limiting for H^+/peptide cotransport. This is in agreement with the observation that different peptides are translocated at very similar I_{max}: The type of peptide may affect binding and rate constants within the loaded carrier, but it does not impact the slowest rate within the transport cycle.

However, different peptides show different K_M-values, defining the substrate specificity in hPepT1. The K_M-value is a result of the combination of rate constants within the substrate translocation pathway [56]. Rate constants are affected due to different interactions of the peptides with the transporter along the translocation pathway, leading to different energy barriers for the conformational transitions. As a side note and opposing to the Na^+/sugar cotransporter SGLT1 [19,20], K_D values, i.e. *real* peptide affinities reflecting the thermodynamics of transporter-substrate interactions are not accessible due to the lack of peptide induced pre steady-state currents (Fig. 1C).

After peptide release in the inward open conformation, the proton is released from its binding site. The equilibrium of proton release is affected by internal pH [61]. In the acidic pH range, I_{max} is massively reduced due to a shift of the proton release equilibrium (see Fig. 3C). This equilibrium affects the rate of alternating access of the empty carrier (Scheme 1, steps V, VI to I). Since major conformational transitions are slow compared to binding equilibria [62], the alternating access of the empty carrier seems to be the major rate limiting step during H^+/peptide cotransport. As a consequence, the overall turnover is limited irrespective of substrate composition, in agreement with very similar I_{max} values across substrates. Therefore, in the context of rational drug design, optimizing affinity and outcompeting other substrates seems crucial for maximizing uptake.

5.7. High-throughput studies promote pharmacological studies

Finally, we investigated the effect of inhibitors on GlyGly transport (Fig. 5), and found that results obtained using the high throughput platform are comparable with those obtained from recordings using the single-well platform, indicating transferability of the procedure. We also found parameters for drug interaction to be similar to the ones obtained by other methods (see above). This opens the door for reliable broad scale compound testing. Thus, the ability to conduct HTS is highly conducive for in-depth multi-parameter studies as well as drug development.

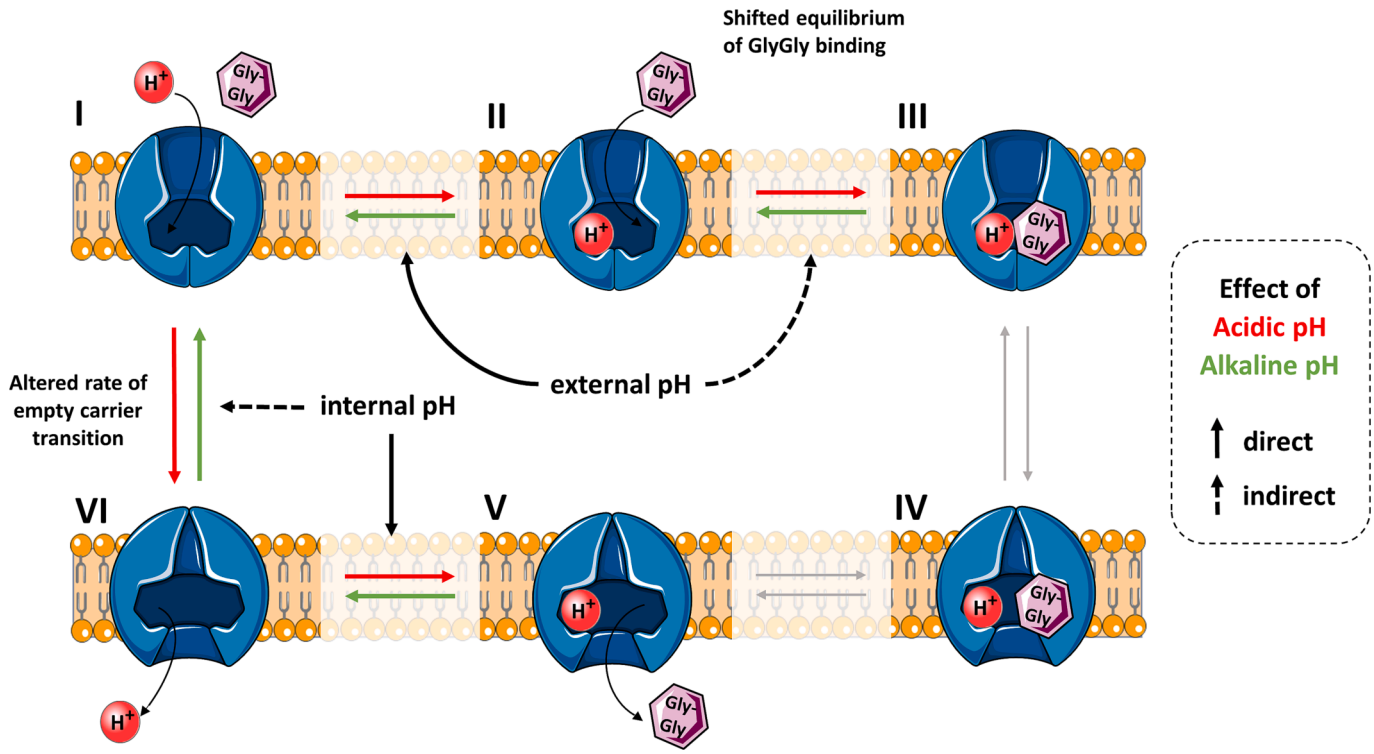

Scheme 1. Incorporation of experimental data into the 6-state transport model. Red arrows indicate transitions being accelerated by acidic pH, whereas green arrows show transitions being accelerated at alkaline pH. Black arrows highlight direct effects, and dashed black arrows indirect effects of pH. The cycle begins in the outward open state (I), the transporter becomes proton-bound (II), before the substrate is able to bind. From fully bound in the outward facing state (III), it transitions inwards (IV). After dissociation of the substrate (V), the transporter may become deprotonated (VI), before the empty inward-facing carrier can transition outwards to initiate the cycle anew. Low external pH facilitates the transition from (I) to (II) directly, and from (II) to (III) indirectly due to the apparent strict binding order and the increased availability of the proton-bound carrier. The opposite is true for alkaline conditions; a low ratio of H^+-bound vs unbound carrier impairs substrate binding capabilities. The result is a low apparent affinity for the peptide (compare Fig. 3B). A high internal pH on the other hand facilitates deprotonation directly and increases the rate of the outward transition indirectly. The opposite is true for acidic conditions. Since the outward transition is the rate limiting step of the transport cycle, changes of the internal pH affect the overall turnover rate (I_{max}, compare Fig. 3C).

6. Conclusions

Concluding, we applied SSME to characterize the transport kinetics in hPepT1. As opposed to many *in-vivo* models and clamp setups, these data were obtained independent of the presence of voltage, but rather as a direct result of substrate addition, yielding a distinct substrate-specific transport response. Apparent substrate affinity is strongly dependent on pH and side-chain composition, supporting the general notion that (a) peptides and even competitive inhibitors may only bind to the protonated carrier, (b) structure, polarity and charge of the substrate strongly affect the apparent affinity of H^+/peptide cotransport, and (c) the deprotonation step affects the return of the empty carrier which is rate-limiting. Based on these results, we developed compound assays for the identification of inhibitors using the single well instrument. We then transferred the assay to the 96-sensor well-plate format that is suitable for drug screening and demonstrated that assays are easily transferable across both instruments.

Overall, the extent to which our findings match to previous studies is arguably surprising. Each method has unique characteristics, and the results therefore sometimes vary drastically. The best way to approach this problem is to be as precise and deliberate as possible about the conditions used, e.g. ion and substrate concentrations, degree of saturation, pH, and voltage. Robust HTS approaches therefore pave the way for in-depth studies with multiple parameters.

CRediT authorship contribution statement

Alexander Körner: Conceptualization, Methodology, Formal analysis, Investigation, Writing – original draft, Writing – review & editing, Supervision, Project administration. **Andre Bazzone:** Methodology, Formal analysis, Investigation, Writing – original draft, Writing – review & editing. **Maximilian Wichert:** Methodology, Formal analysis, Writing – review & editing. **Maria Barthmes:** Writing – review & editing. **Srujan Kumar Dondapati:** Conceptualization, Supervision, Project administration, Writing – review & editing. **Niels Fertig:** Resources, Funding acquisition. **Stefan Kubick:** Supervision, Funding acquisition.

Declaration of Competing Interest

The authors declare the following financial interests/personal relationships which may be considered as potential competing interests: Authors AB, MB and NF are employed by Nanion Technologies GmbH, the developer of the SURFE^{2}R instruments.

Data availability

Data will be made available on request.

Acknowledgements

Parts of schematic illustrations in Fig. 1, and figure SI-1 were created with BioRender.com. Parts of figure 1, 3, 5, SI-1, Scheme 1 and the graphical abstract were drawn by using pictures from Servier Medical Art. Servier Medical Art by Servier is licensed under a Creative Commons Attribution 3.0 Unported License (https://creativecommons.org/licenses/by/3.0/).

This research was supported by the European Regional Development Fund and the German Ministry of Education and Research (BMBF, Nos.

13GW0408C) and Ministry of Science, Research and Culture (MWFK, Brandenburg, Germany), project PZ-Syn (project number F241-03-FhG/005/001).

Appendix A. Supplementary material

Supplementary data to this article can be found online at https://doi.org/10.1016/j.bioelechem.2023.108573.

References

[1] G.S. Minhas, S. Newstead, Recent advances in understanding prodrug transport through the SLC15 family of proton-coupled transporters, Biochem. Soc. Trans. 48 (2020) 337–346.
[2] H. Daniel, G. Kottra, The proton oligopeptide cotransporter family SLC15 in physiology and pharmacology, Pflugers Arch. 447 (2004) 610–618.
[3] D.E. Smith, B. Clémençon, M.A. Hediger, Proton-coupled oligopeptide transporter family SLC15: physiological, pharmacological and pathological implications, Mol. Aspects Med. 34 (2013) 323–336.
[4] M. Stauffer, J.-M. Jeckelmann, H. Ilgü, Z. Ucurum, R. Boggavarapu, D. Fotiadis, Peptide transporter structure reveals binding and action mechanism of a potent PEPT1 and PEPT2 inhibitor, Commun Chem 5 (2022).
[5] G. Kottra, A. Stamfort, H. Daniel, PEPT1 as a paradigm for membrane carriers that mediate electrogenic bidirectional transport of anionic, cationic, and neutral substrates, J. Biol. Chem. 277 (2002) 32683–32691.
[6] D. Meredith, Review., The mammalian proton-coupled peptide cotransporter PepT1: sitting on the transporter-channel fence? Philos. Trans. R. Soc. Lond. B Biol. Sci. 364 (2009) 203–207.
[7] Y. Ural-Blimke, A. Flayhan, J. Strauss, V. Rantos, K. Bartels, R. Nielsen, E. Pardon, J. Steyaert, J. Kosinski, E.M. Quistgaard, C. Löw, Structure of Prototypic Peptide Transporter DtpA from E. coli in Complex with Valganciclovir Provides Insights into Drug Binding of Human PepT1, J. Am. Chem. Soc. 141 (2019) 2404–2412.
[8] M.E. Ganapathy, P.D. Prasad, B. Mackenzie, V. Ganapathy, F.H. Leibach, Interaction of anionic cephalosporins with the intestinal and renal peptide transporters PEPT 1 and PEPT 2, Biochimica et Biophysica Acta (BBA) - Biomembranes 1324 (1997) 296–308.
[9] P. Luckner, M. Brandsch, Interaction of 31 beta-lactam antibiotics with the H+/peptide symporter PEPT2: analysis of affinity constants and comparison with PEPT1, European journal of pharmaceutics and biopharmaceutics official journal of Arbeitsgemeinschaft fur Pharmazeutische Verfahrenstechnik e.V 59 (2005) 17–24.
[10] M. Brandsch, Drug transport via the intestinal peptide transporter PepT1, Curr. Opin. Pharmacol. 13 (2013) 881–887.
[11] M. Brandsch, I. Knütter, E. Bosse-Doenecke, Pharmaceutical and pharmacological importance of peptide transporters, J. Pharm. Pharmacol. 60 (2008) 543–585.
[12] J. Zhang, H. Wen, F. Shen, X. Wang, C. Shan, C. Chai, J. Liu, W. Li, Synthesis and biological evaluation of a novel series of curcumin-peptide derivatives as PepT1-mediated transport drugs, Bioorg. Chem. 92 (2019), 103163.
[13] B. Spanier, Transcriptional and functional regulation of the intestinal peptide transporter PEPT1, J. Physiol. 592 (2014) 871–879.
[14] J.H. Beale, J.L. Parker, F. Samsudin, A.L. Barrett, A. Senan, L.E. Bird, D. Scott, R. J. Owens, M.S.P. Sansom, S.J. Tucker, D. Meredith, P.W. Fowler, S. Newstead, Crystal Structures of the Extracellular Domain from PepT1 and PepT2 Provide Novel Insights into Mammalian Peptide Transport, Structure (London, England 23 (2015) (1993) 1889–1899.
[15] N. Solcan, J. Kwok, P.W. Fowler, A.D. Cameron, D. Drew, S. Iwata, S. Newstead, Alternating access mechanism in the POT family of oligopeptide transporters, EMBO J. 31 (2012) 3411–3421.
[16] P.D. Bosshart, D. Fotiadis, Secondary Active Transporters, Subcell. Biochem. 92 (2019) 275–299.
[17] E.M. Quistgaard, C. Löw, F. Guettou, P. Nordlund, Understanding transport by the major facilitator superfamily (MFS): structures pave the way, Nat. Rev. Mol. Cell Biol. 17 (2016) 123–132.
[18] G. Kottra, H. Daniel, Bidirectional electrogenic transport of peptides by the proton-coupled carrier PEPT1 in Xenopus laevis oocytes: its asymmetry and symmetry, J. Physiol. 536 (2001) 495–503.
[19] A. Bazzone, A. Körner, M. Meincke, M. Bhatt, S. Dondapati, M. Barthmes, S. Kubick, N. Fertig, SSM-based electrophysiology, a label-free real-time method reveals sugar binding & transport events in SGLT1, Biosens. Bioelectron. 197 (2022), 113763.
[20] A. Bazzone, R. Zerlotti, M. Barthmes, N. Fertig, Functional characterization of SGLT1 using SSM-based electrophysiology: Kinetics of sugar binding and translocation, Front. Physiol. 14 (2023).
[21] A. Bazzone, M. Barthmes, C. George, N. Brinkwirth, R. Zerlotti, V. Prinz, K. Cole, S. Friis, A. Dickson, S. Rice, J. Lim, M. Fern Toh, M. Mohammadi, D. Pau, D.J. Stone, J.J. Renger, N. Fertig, A Comparative Study on the Lysosomal Cation Channel TMEM175 Using Automated Whole-Cell Patch-Clamp, Lysosomal Patch-Clamp, and Solid Supported Membrane-Based Electrophysiology: Functional Characterization and High-Throughput Screening Assay Development, International journal of molecular sciences 24 (2023).
[22] A. Bazzone, M. Barthmes, K. Fendler, SSM-Based Electrophysiology for Transporter Research, Methods Enzymol. 594 (2017) 31–83.
[23] M. Rafiq, H.A. Ernst, N.G. Aduri, B.K. Prabhala, S. Tufail, M. Rahman, M.B. Bloch, N. Mirza, N.M.I. Taylor, T. Boesen, M. Gajhede, O. Mirza, Expression, purification and characterization of human proton-coupled oligopeptide transporter 1 hPEPT1, Protein Expr. Purif. 190 (2022), 105990.
[24] C. Gerbeth-Kreul, A. Pommereau, S. Ruf, J.L. Kane, T. Kuntzweiler, G. Hessler, C. K. Engel, P. Shum, L. Wei, J. Czech, T. Licher, A Solid Supported Membrane-Based Technology for Electrophysical Screening of B0AT1-Modulating Compounds, SLAS discovery advancing life sciences R & D 26 (2021) 783–797.
[25] M. Stauffer, Z. Ucurum, D. Harder, D. Fotiadis, Engineering and functional characterization of a proton-driven β-lactam antibiotic translocation module for bionanotechnological applications, Sci. Rep. 11 (2021) 17205.
[26] A. Bazzone, M. Barthmes, Functional Characterization of SLC Transporters Using Solid Supported Membranes, Methods in molecular biology 2168 (2020) 73–103.
[27] R. Gesztelyi, J. Zsuga, A. Kemeny-Beke, B. Varga, B. Juhasz, A. Tosaki, The Hill equation and the origin of quantitative pharmacology, Arch. Hist. Exact Sci. 66 (2012) 427–438.
[28] S. Nussberger, A. Steel, D. Trotti, M.F. Romero, W.F. Boron, M.A. Hediger, Symmetry of H+ binding to the intra- and extracellular side of the H+-coupled oligopeptide cotransporter PepT1, J. Biol. Chem. 272 (1997) 7777–7785.
[29] B. Mackenzie, Y.-J. Fei, V. Ganapathy, F.H. Leibach, The human intestinal H+/oligopeptide cotransporter hPEPT1 transports differently-charged dipeptides with identical electrogenic properties, Biochimica et Biophysica Acta (BBA) -, Biomembranes (1996, 1284,) 125–128.
[30] J.L. Parker, J.A. Mindell, S. Newstead, Thermodynamic evidence for a dual transport mechanism in a POT peptide transporter eLife 3 (2014).
[31] R.M. Kennedy, Hydrophobic chromatography, Methods Enzymol. 182 (1990) 339–343.
[32] I. Knütter, S. Theis, B. Hartrodt, I. Born, M. Brandsch, H. Daniel, K. Neubert, A novel inhibitor of the mammalian peptide transporter PEPT1, Biochemistry 40 (2001) 4454–4458.
[33] K. Sawada, T. Terada, H. Saito, Y. Hashimoto, K. Inui, Effects of glibenclamide on glycylsarcosine transport by the rat peptide transporters PEPT1 and PEPT2, Br. J. Pharmacol. 128 (1999) 1159–1164.
[34] Y.A. Pak, A.J. Long, W.F. Annes, J.W. Witcher, M.P. Knadler, M.A. Ayan-Oshodi, M.I. Mitchell, P. Leese, K.M. Hillgren, In Vitro and Clinical Evaluations of the Drug-Drug Interaction Potential of a Metabotropic Glutamate 2/3 Receptor Agonist Prodrug with Intestinal Peptide Transporter 1, Drug metabolism and disposition: the biological fate of chemicals 45 (2017) 137–144.
[35] J. Neumann, M. Bruch, S. Gebauer, M. Brandsch, Transport of the phosphonodipeptide alafosfalin by the H+/peptide cotransporters PEPT1 and PEPT2 in intestinal and renal epithelial cells, Eur. J. Biochem. 271 (2004) 2012–2017.
[36] M. Okamura, T. Terada, T. Katsura, H. Saito, K. Inui, Inhibitory effect of zinc on PEPT1-mediated transport of glycylsarcosine and beta-lactam antibiotics in human intestinal cell line Caco-2, Pharm. Res. 20 (2003) 1389–1393.
[37] V. Kotov, M. Killer, K.E.J. Jungnickel, J. Lei, G. Finocchio, J. Steinke, K. Bartels, J. Strauss, F. Dupeux, A.-S. Humm, I. Cornaciu, J.A. Márquez, E. Pardon, J. Steyaert, C. Löw, Plasticity of the binding pocket in peptide transporters underpins promiscuous substrate recognition, Cell Rep. 42 (2023), 112831.
[38] D.W. Foley, J. Rajamanickam, P.D. Bailey, D. Meredith, Bioavailability through PepT1: the role of computer modelling in intelligent drug design, Curr. Comput. Aided Drug Des. 6 (2010) 68–78.
[39] M.E. Ganapathy, et al., Valacyclovir: A Substrate for the Intestinal and Renal Peptide Transporters PEPT1 and PEPT2, Biochem. Biophys. Res. Commun. 246 (1998) 470–475.
[40] G.S. Minhas, S. Newstead, Structural basis for prodrug recognition by the SLC15 family of proton-coupled peptide transporters, Proceedings of the National Academy of Sciences of the United States of America 116 (2019) 804–809.
[41] A. Bazzone, L. Tesmer, D. Kurt, H.R. Kaback, K. Fendler, M.G. Madej, Investigation of sugar binding kinetics of the E. coli sugar/H+ symporter XylE using solid-supported membrane-based electrophysiology, J. Biol. Chem. 298 (2022), 101505.
[42] A. Omori, Y. Fujisawa, S. Sasaki, K. Shimono, T. Kikukawa, S. Miyauchi, Protonation State of a Histidine Residue in Human Oligopeptide Transporter 1 (hPEPT1) Regulates hPEPT1-Mediated Efflux Activity, Biol. Pharm. Bull. 44 (2021) 678–685.
[43] A. Bazzone, M.G. Madej, H.R. Kaback, K. Fendler, pH Regulation of Electrogenic Sugar/H+ Symport in MFS Sugar Permeases, PLoS One 11 (2016) e0156392.
[44] M. Pieri, D. Hall, R. Price, P. Bailey, D. Meredith, Site-directed mutagenesis of Arginine282 suggests how protons and peptides are co-transported by rabbit PepT1, Int. J. Biochem. Cell Biol. 40 (2008) 721–730.
[45] J.R. Kunta, P.J. Sinko, Intestinal drug transporters: in vivo function and clinical importance, Curr. Drug Metab. 5 (2004) 109–124.
[46] B. Dhanalakshmi, B. Sailaja, Protonation equilibria of glycylglycine and histamine in aqueous solution of an anionic surfactant, Chem. Spec. Bioavailab. 26 (2014) 52–58.
[47] J.T. Edsall, J. Wyman, Biophysical Chemistry, Academic Press, New York, 1958.
[48] M. Sala-Rabanal, D.D.F. Loo, B.A. Hirayama, E. Turk, E.M. Wright, Molecular interactions between dipeptides, drugs and the human intestinal H+ -oligopeptide cotransporter hPEPT1, J. Physiol. 574 (2006) 149–166.
[49] D. Foley, P. Bailey, M. Pieri, D. Meredith, Targeting ketone drugs towards transport by the intestinal peptide transporter, PepT1, Org. Biomol. Chem. 7 (2009) 1064–1067.
[50] F. Vacca, A. Barca, A.S. Gomes, A. Mazzei, B. Piccinni, R. Cinquetti, G. Del Vecchio, A. Romano, I. Rønnestad, E. Bossi, T. Verri, The peptide transporter 1a of the zebrafish Danio rerio, an emerging model in nutrigenomics and nutrition research:

molecular characterization, functional properties, and expression analysis, Genes Nutr. 14 (2019) 33.
[51] I.H. Madshus, Regulation of intracellular pH in eukaryotic cells, Biochem. J. 250 (1988) 1–8.
[52] J. Fallingborg, Intraluminal pH of the human gastrointestinal tract, Dan. Med. Bull. 46 (1999) 183–196.
[53] K. Ito, A. Hikida, S. Kawai, V.T.T. Lan, T. Motoyama, S. Kitagawa, Y. Yoshikawa, R. Kato, Y. Kawarasaki, Analysing the substrate multispecificity of a proton-coupled oligopeptide transporter using a dipeptide library, Nat. Commun. 4 (2013) 2502.
[54] Q. Xu, Z. Liu, H. Liu, F. Zhao, X. Huang, Y. Wu, J. Liu, Functional characterization of oligopeptide transporter 1 of dairy cows, J. Anim. Sci. Biotechnol. 9 (2018) 7.
[55] A. Steel, S. Nussberger, M.F. Romero, W.F. Boron, C.A. Boyd, M.A. Hediger, Stoichiometry and pH dependence of the rabbit proton-dependent oligopeptide transporter PepT1, J. Physiol. 498 (Pt 3) (1997) 563–569.
[56] K.A. Johnson, New standards for collecting and fitting steady state kinetic data, Beilstein J. Org. Chem. 15 (2019) 16–29.
[57] P.D. Bailey, C.A. Boyd, J.R. Bronk, I.D. Collier, D. Meredith, K.M. Morgan, C. S. Temple, How to Make Drugs Orally Active: A Substrate Template for Peptide Transporter PepT1, Angew. Chem. 2000 (2000) 515–518.
[58] T. Uchiyama, A.A. Kulkarni, D.L. Davies, V.H.L. Lee, Biophysical evidence for His57 as a proton-binding site in the mammalian intestinal transporter hPepT1, Pharm. Res. 20 (2003) 1911–1916.
[59] J.L. Parker, C. Li, A. Brinth, Z. Wang, L. Vogeley, N. Solcan, G. Ledderboge-Vucinic, J.M.J. Swanson, M. Caffrey, G.A. Voth, S. Newstead, Proton movement and coupling in the POT family of peptide transporters, Proceedings of the National Academy of Sciences of the United States of America 114 (2017) 13182–13187.
[60] S. Newstead, D. Drew, A.D. Cameron, V.L.G. Postis, X. Xia, P.W. Fowler, J. C. Ingram, E.P. Carpenter, M.S.P. Sansom, M.J. McPherson, S.A. Baldwin, S. Iwata, Crystal structure of a prokaryotic homologue of the mammalian oligopeptide-proton symporters, PepT1 and PepT2, EMBO J. 30 (2011) 417–426.
[61] D. Meredith, R.W. Laynes, Dipeptide transport in brush-border membrane vesicles (BBMV) prepared from human full-term placentae, Placenta 17 (1996) 173–179.
[62] L.R. Forrest, R. Krämer, C. Ziegler, The structural basis of secondary active transport mechanisms, BBA 2011 (1807) 167–188.